

Creative Commons Attribution 4.0 International (CC BY 4.0 DEED)

<https://creativecommons.org/licenses/by/4.0/>

Access to this work was provided by the University of Maryland, Baltimore County (UMBC) ScholarWorks@UMBC digital repository on the Maryland Shared Open Access (MD-SOAR) platform.

Please provide feedback

Please support the ScholarWorks@UMBC repository by emailing scholarworks-group@umbc.edu and telling us what having access to this work means to you and why it's important to you. Thank you.

Incorporation of realistic intrinsic profiles for the Fe $K\alpha$ and Fe $K\beta$ emission lines in X-ray reprocessor models

Tahir Yaqoob^{1,2★}

¹Center for Space Science and Technology, University of Maryland, Baltimore County, 1000 Hilltop Circle, Baltimore, MD 21250, USA

²Center for Research and Exploration in Space Science and Technology, NASA/GSFC, Mail Code 662, Greenbelt, MD 20771, USA

Accepted 2023 October 17. Received 2023 October 12; in original form 2023 September 18

ABSTRACT

The Fe $K\alpha$ fluorescent emission line from neutral matter is widely used as a diagnostic tool in X-ray spectroscopy for many astrophysical X-ray sources. The line properties can potentially be used to constrain the geometry, column density, and kinematics of the material in which the line is formed. The intrinsic width and the shape of the intrinsic line profile has been neglected thus far, because it is much smaller than the instrumental broadening in all space-based X-ray detectors before *Hitomi*. However, the instrumental broadening of X-ray microcalorimeters is comparable to the intrinsic line width. We have performed new calculations based on Monte Carlo simulations of the MYTORUS X-ray reprocessor spectral-fitting model that utilize parametrizations of historical high-precision laboratory measurements of the intrinsic profiles of the Fe $K\alpha$ and Fe $K\beta$ lines. A publicly available table is provided that can seamlessly replace the existing Fe $K\alpha$ and Fe $K\beta$ line spectrum in the MYTORUS model. The new table can also be used in a standalone mode (without the MYTORUS model) in order to derive empirical velocity widths, if the line-emitting matter is Compton thin. Neglecting to account for the intrinsic profiles of the Fe $K\alpha$ and Fe $K\beta$ lines can result in a significant overestimate of the velocity broadening, if the true velocity broadening is less than $\sim 2000 \text{ km s}^{-1}$. Residual artefacts may also appear in observed line profiles in data with a high signal-to-noise ratio.

Key words: line: profiles – radiation mechanisms: general – galaxies: active – X-rays: binaries – X-rays: general.

1 INTRODUCTION

A narrow, fluorescent Fe $K\alpha$ emission line from neutral matter, centred at $\sim 6.4 \text{ keV}$, is now well established as a powerful probe of the geometry, physical conditions, and kinematics in many astrophysical sources. Here, ‘narrow’ is defined by a full width at half-maximum (FWHM) velocity that is less than $\sim 10\,000 \text{ km s}^{-1}$. Although this velocity is arbitrary, the general defining feature is that relativistic effects can be neglected, and this FWHM corresponds to $(v/c) \sim 3$ per cent. The narrow Fe $K\alpha$ line has been detected in many active galactic nuclei (Sulentic et al. 1998; Lubiński & Zdziarski 2001; Yaqoob & Padmanabhan 2004; Shu, Yaqoob & Wang 2010, 2011; Andonie et al. 2022, and references therein) is observed in X-ray binaries (Torrejón et al. 2010; Tzanavaris & Yaqoob 2018, and references therein), and has also been detected in diffuse emission from the Galactic Centre (e.g. Nobukawa et al. 2016). The Fe $K\beta$ line can provide additional constraints for X-ray spectral modelling, but statistically significant detections of the line are rare because it is an order of magnitude weaker than the Fe $K\alpha$ line. Examples of significant detections that have been reported are the Seyfert galaxy NGC 2992 (Yaqoob et al. 2007), the accreting X-ray pulsar OAO 1657–415 (Pradhan, Raman & Paul 2019), and the Circinus galaxy (Andonie et al. 2022, and references therein).

Hölzer et al. (1997; hereafter H97) performed high-precision laboratory measurements of the Fe $K\alpha$ and Fe $K\beta$ line profiles, and found that the two components of the Fe $K\alpha$ line, $K\alpha_1$ (at 6.404 keV) and $K\alpha_2$ (at 6.391 keV), have FWHM values of 2.55 and 3.14 eV, respectively. They also measured the FWHM of Fe $K\beta$ (at 7.058 keV) to be 3.53 eV. These line widths are negligible compared to the spectral resolution of X-ray CCD spectrometers (FWHM $\sim 150 \text{ eV}$ at 6.4 keV , e.g. Koyama et al. 2007), and the spectral resolution of the Cadmium-Zinc-Telluride *NuSTAR* detectors (FWHM $\sim 400 \text{ eV}$ at 6.4 keV ; Harrison et al. 2013). The line widths are an order of magnitude smaller than the spectral resolution of the *Chandra* high-energy grating (FWHM $\sim 39 \text{ eV}$; Markert et al. 1994; Yaqoob & Padmanabhan 2004). Therefore, due to the comparatively large instrumental broadening, the intrinsic widths of the Fe $K\alpha$ and Fe $K\beta$ lines have been universally neglected in the modelling of X-ray spectra. However, X-ray microcalorimeters will now usher in a new era for X-ray spectroscopy, because the spectral resolution at 6.4 eV is in the range $\sim 4\text{--}7 \text{ eV}$, corresponding to an equivalent velocity broadening of $\sim 200\text{--}350 \text{ km s}^{-1}$. Therefore, the intrinsic widths of the Fe $K\alpha$ and Fe $K\beta$ lines cannot be neglected when modelling microcalorimeter X-ray data.

Alongside improvements in X-ray detectors and telescopes, a number of models have been developed that self-consistently account for reprocessing of the X-ray continuum by the same material that produces the Fe $K\alpha$ emission line, as well as other fluorescent line features (Ikeda, Awaki & Terashima 2009; Murphy & Yaqoob 2009; Brightman & Nandra 2011; Liu & Li 2014; Furui et al. 2016;

★ E-mail: tahir@umbc.edu

Baloković 2018; Buchner et al. 2019; Tanimoto et al. 2019; Saha, Markowitz & Buchner 2022, and references therein). Here, X-ray reprocessing generally refers to absorption and Compton scattering of the incident continuum, and inner shell line emission. All of these models neglect the intrinsic widths of the fluorescent emission lines. For example, in the MYTORUS X-ray reprocessor model (Murphy & Yaqoob 2009), which has been widely used to model X-ray spectra of active galactic nuclei, the Fe $K\alpha$ line is treated using a pair of simple Gaussian profiles with an FWHM of only 10 km s^{-1} , and the Fe $K\beta$ line is treated as a single line with the same FWHM.

In this paper, we report on an upgrade to the publicly available MYTORUS model that is a result of new calculations based on Monte Carlo simulations for the MYTORUS model, that incorporate the H97 precision laboratory measurements of the intrinsic Fe $K\alpha$ and Fe $K\beta$ line profiles. A new line table model is provided that can seamlessly replace the existing MYTORUS line table model (or a variant of it), that is based on the simpler prescription of the line widths (hereafter, we refer to the older table as the ‘standard’ line table). H97 modelled the Fe $K\alpha_1$, Fe $K\alpha_2$, and Fe $K\beta$ components with four, three, and four Lorentzians, respectively. We adopted this eleven-Lorentzian parametrization for the intrinsic Fe $K\alpha$ and Fe $K\beta$ line spectrum in the newMYTORUS simulations.

The remainder of the paper is organized as follows. In Section 2, we give details of the new Fe $K\alpha$ and Fe $K\beta$ line spectrum table and show the intrinsic line profiles without the effects of Compton-scattering, absorption, velocity broadening, and instrumental broadening. In Section 3, we discuss the effects of velocity broadening. In Section 4, we show the results of some simulations that include both the effects of velocity broadening, and instrument broadening corresponding to typical X-ray microcalorimeter spectral resolution. Our results and conclusions are summarized in Section 5.

2 A NEW LINE TABLE FOR THE MYTORUS MODEL

The MYTORUS model (Murphy & Yaqoob 2009) has been extensively used in the literature to perform X-ray spectral fitting of X-ray spectra of sources with narrow Fe $K\alpha$ (and in some cases Fe $K\beta$) fluorescent lines from neutral Fe, in order to self-consistently account for the fluorescent lines and the associated Compton-scattered continuum (e.g. LaMassa et al. 2014; Yaqoob et al. 2015, 2016, 2023; Miller et al. 2019; Andonie et al. 2022, and references therein). The model enables two column densities to be derived from X-ray spectra, one for the line of sight (l.o.s.), and one that is due to matter out of the l.o.s. (see Yaqoob 2012 and Yaqoob et al. 2015). The two column densities may or may not be similar, and they give insight into the global distribution of the reflecting and line-emitting matter.

The MYTORUS model consists of three FITS tables that work in unison to operate on an incident power-law continuum spectrum to generate a reprocessed X-ray spectrum for a given torus equatorial column density and inclination angle. The three tables correspond to (1) the l.o.s. extinction (due to absorption and scattering), to generate what is known as the ‘zeroth order’ continuum, (2) the Compton-scattered continuum, and (3) the Fe $K\alpha$ and Fe $K\beta$ fluorescent emission lines. Up to now, the emission-line table has been based on simple Gaussian intrinsic line profiles for Fe $K\alpha_1$, Fe $K\alpha_2$, and Fe $K\beta$, that have negligible widths (10 km s^{-1} FWHM) compared to even the highest spectral resolution space-based X-ray detector available ($\sim 200\text{--}350 \text{ km s}^{-1}$ FWHM at 6.4 keV, for microcalorimeters). We have applied the same Monte Carlo techniques and methods

described in Murphy & Yaqoob (2009) to calculate a new line table based on the H97 intrinsic line profiles. No additional velocity broadening is applied (arbitrary velocity broadening can be applied by using a Gaussian convolution model during the spectral-fitting process). The new line table, `myt1_V000HLZnEp000_v00.fits`, is available to download.¹ The new table, hereafter referred to as the HLZ table model, can simply replace the standard line table and seamlessly work with the existing zeroth order continuum and Compton-scattered continuum tables. All the methods in the literature for using the MYTORUS model, including spectral-fitting model expressions, still apply when the new line table replaces the standard line table. Whilst Compton-scattered continuum tables for MYTORUS are available for different high-energy cut-offs, in the range 100–500 keV, only one line table is required, because the Fe $K\alpha$ and Fe $K\beta$ line profiles are insensitive to the high-energy cut-off in the range covered by the supplied Compton-scattered continuum tables. Therefore, the new line table can be used with any of the MYTORUS continuum tables (for a power-law intrinsic continuum).

As with the standard MYTORUS line table, the new line table model covers a range in the intrinsic power-law continuum photon index of 1.4–2.6, a range in the inclination angle of 0° to 90° , and a range in the column density of $10^{22}\text{--}10^{25} \text{ cm}^{-2}$. At the smallest column density, the matter is optically thin to Compton scattering and to absorption at the energies covering the line profiles of Fe $K\alpha_1$, Fe $K\alpha_2$, and Fe $K\beta$. Since the effects of Compton scattering and differential absorption across the line profiles are negligible, the fluorescent emission-line profiles are essentially just the intrinsic H97 line profiles at the lowest column density in the new line table. In addition, since the matter in this regime is optically thin to Compton scattering and absorption, the line profiles are insensitive to the inclination angle. Fig. 1 shows the Fe $K\alpha$ and Fe $K\beta$ line profiles from the new MYTORUS line table for a column density of 10^{22} cm^{-2} . The intrinsic widths of the Fe $K\alpha$ components and the Fe $K\beta$ line even without any velocity broadening, instrumental broadening, or broadening due to Compton scattering, are comparable to microcalorimeter spectral resolution. The FWHM values reported by H97 for Fe $K\alpha_1$, Fe $K\alpha_2$, and Fe $K\beta$ are equivalent to ~ 120 , 150, and 140 km s^{-1} , respectively.

At the highest column density in the MYTORUS line tables, 10^{25} cm^{-2} , the matter is Compton thick, with a Thomson depth of ~ 8 , and the effects of Compton downscattering are imprinted on the Fe $K\alpha$ and Fe $K\beta$ line profiles, forming the so-called Compton shoulder (e.g. see Matt et al. (e.g. see Matt et al. 2004; Yaqoob & Murphy 2011; Furui et al. 2016; Odaka et al. 2016; Hikitani et al. 2018). This is illustrated in Fig. 2 for an inclination angle of 90° . For these parameters, the Compton shoulder carries ~ 20 per cent of the flux in the unscattered line core (e.g. see Murphy & Yaqoob 2009; Yaqoob & Murphy 2011), and it peaks at the lowest energy of the first scattering, at $\sim 6.24 \text{ keV}$ for the Fe $K\alpha$ line, and at $\sim 6.87 \text{ keV}$ for the Fe $K\beta$ line.

2.1 General applicability of the new line table

The MYTORUS model is not strictly confined to modelling an X-ray reprocessor with a toroidal geometry. It can also crudely emulate other geometries when it is used in so-called decoupled mode (e.g. Yaqoob 2012). The new MYTORUS line table can be used in both coupled and decoupled modes, in the same way as the standard line table is used.

¹<http://mytorus.com/mytfiles.html>

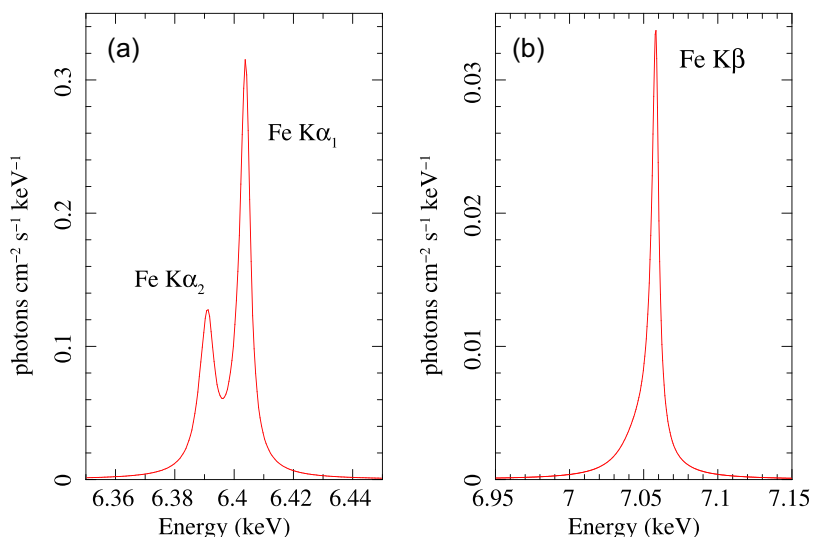


Figure 1. The Hölzer et al. (1997) intrinsic emission-line profiles implemented in the MYTORUS model ($N_H = 10^{22} \text{ cm}^{-2}$, inclination angle 0°) for (a) Fe $K\alpha$ and (b) Fe $K\beta$. No velocity or instrumental broadening has been applied, and in this limit of low column densities, there are negligible effects of Compton scattering on the line profiles. See text for details.

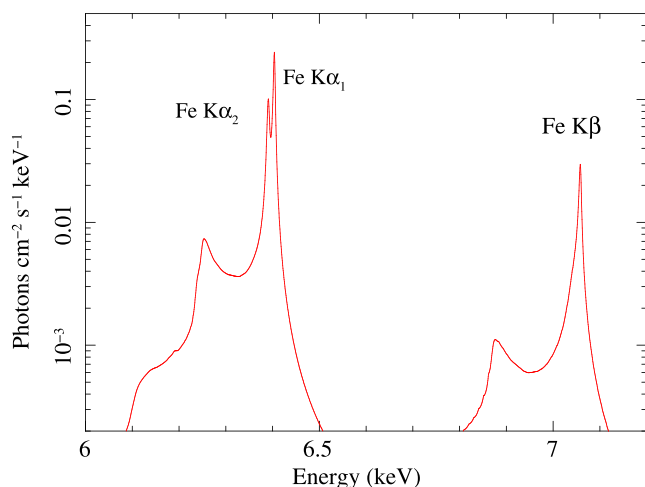


Figure 2. The Hölzer et al. (1997) intrinsic emission-line profiles implemented in the MYTORUS model, in the Compton-thick regime. The model has $N_H = 10^{25} \text{ cm}^{-2}$, and an inclination angle of 90° . No velocity or instrumental broadening has been applied. The effects of Compton scattering form Compton shoulders on the two components of the Fe $K\alpha$ line, and on the Fe $K\beta$ line. See text for details.

There are some data analysis scenarios for which only an empirical line profile is needed to fit to X-ray spectra of the Fe $K\alpha$ and Fe $K\beta$ lines, independent of a physical model of the X-ray reprocessor, in order to obtain a simple, model-independent exploratory determination of the velocity broadening. This can also be done with the new line table model that is based on the Hölzer intrinsic line Fe $K\alpha$ and Fe $K\beta$ line profiles, by fixing the column density at the smallest value in the table (10^{22} cm^{-2}), and fixing the inclination angle at any value between 0° and 90° . At this column density, the line profiles are not sensitive to the photon index of the intrinsic power-law continuum, so the photon index can either be fixed at any value in the permitted range, or it can be tied to the value used for fitting the underlying continuum. Velocity broadening can be

implemented simply by convolving the model line spectrum by a Gaussian kernel (see Section 3).

3 VELOCITY BROADENING

In this section, we illustrate the effects of velocity broadening on intrinsic line profiles based on H97. We used the GSMOOTH Gaussian convolution model in the XSPEC X-ray spectral-fitting package (Arnaud 1996)² to emulate velocity broadening of the Fe $K\alpha$ and Fe $K\beta$ line profiles in the new HLZ line table model described in Section 2. The GSMOOTH model can apply the same velocity FWHM at all energies by making the Gaussian width proportional to energy (e.g. see Yaqoob et al. 2016), so that the same velocity width is applied to both components of the Fe $K\alpha$ line and to the Fe $K\beta$ line. The column density was fixed at 10^{22} cm^{-2} in order to illustrate the effects of velocity broadening on the intrinsic line profiles without the effects of Compton scattering. The effects of velocity broadening and instrumental broadening of line profiles for higher column densities will be illustrated in Section 4. The inclination angle and intrinsic continuum photon index were fixed at 0° and 1.9, respectively, although the line profiles are not sensitive to either of these parameters for a column density of 10^{22} cm^{-2} . Fig. 3 compares the Fe $K\alpha$ line profiles calculated from the new HLZ table directly with the standard MYTORUS line table, both with the same line broadening applied. The results are shown for six values of the FWHM of the velocity broadening: 100, 200, 300, 500, 1000, and 2000 km s^{-1} . The HLZ Fe $K\beta$ line profile is not as complex as that of the Fe $K\alpha$ line, and the corresponding velocity-broadened Fe $K\beta$ line profiles are not shown here, for the sake of brevity.

In Fig. 3, it can be seen that the Fe $K\alpha_1$ and Fe $K\alpha_2$ line components for the HLZ model have become very blended for the line profile with an FWHM of 500 km s^{-1} , whilst the components for the standard model are still distinct. Even for smaller velocity widths, the HLZ Fe $K\alpha_1$ and Fe $K\alpha_2$ line peaks have a lower contrast than the standard model, and the overall HLZ line profile is always broader than that of the standard model. However, the line profiles for both models have

²<http://heasarc.gsfc.nasa.gov/docs/xanadu/xspec/>

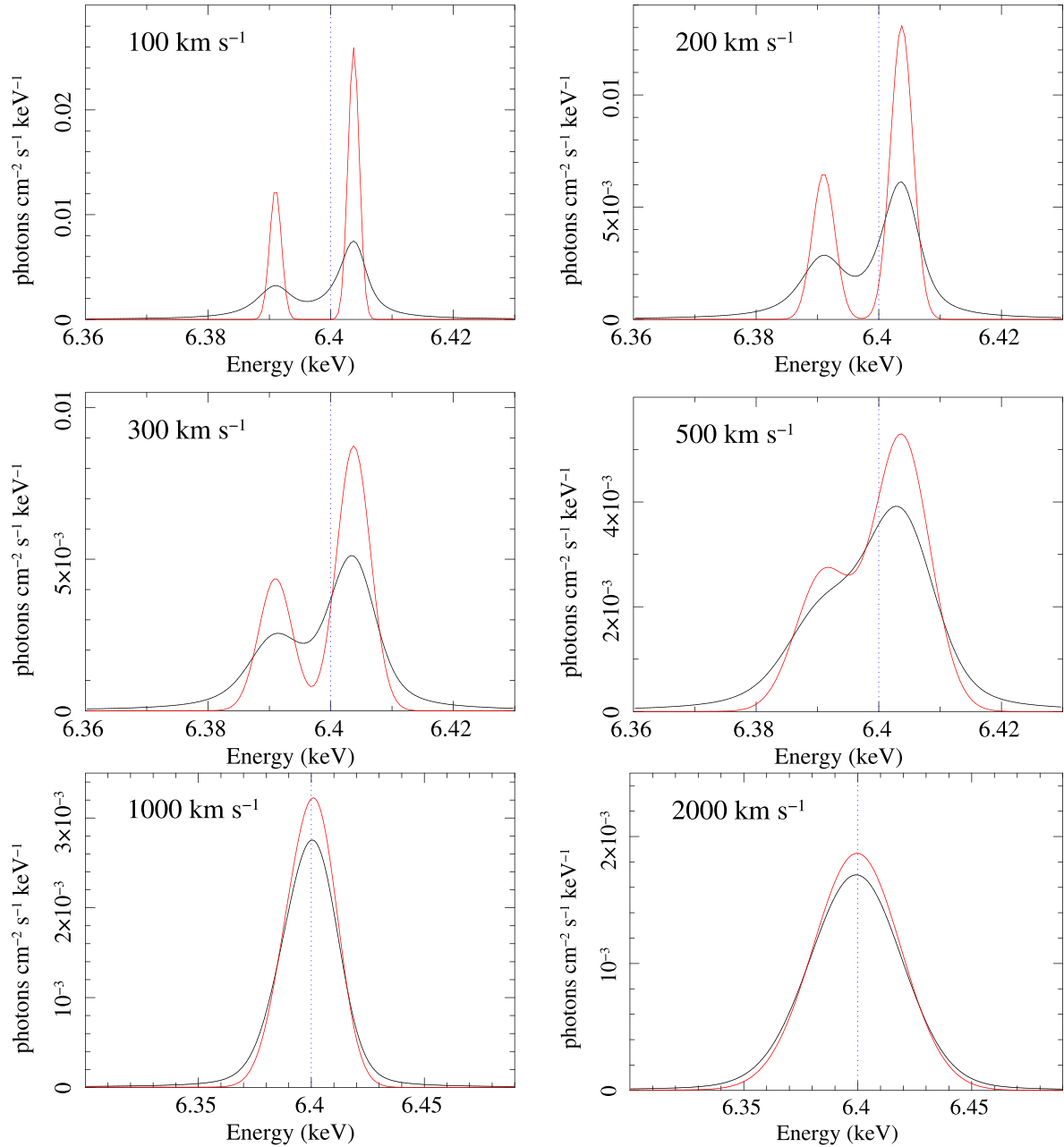


Figure 3. Comparison of the Fe $K\alpha$ line profiles with the Hölzer et al. (1997) and standard Gaussian implementations in the MYTORUS model, for six different velocity broadening FWHM values, for $N_H = 10^{22} \text{ cm}^{-2}$, and an inclination angle of 0° . In this low-column density limit, the line shape is insensitive to the geometry and orientation of the X-ray reprocessor, so the line profile comparisons have a generality that is applicable in the Compton-thin regime. The FWHM values range from 100 to 2000 km s^{-1} , and the value for each pair of line profiles is indicated at the top left of each panel. The dotted lines at 6.4 keV correspond to the weighted mean energy of the peaks of the Fe $K\alpha_1$ and Fe $K\alpha_2$ line components. The line profiles based on the HLZ table are shown in black, and those based on the standard MYTORUS table are shown in red.

blended into a single peak for the case shown with an FWHM of 1000 km s^{-1} , and the overall profile is almost symmetric, peaking at 6.4 keV. The HLZ line profile is somewhat broader than the profile for the simpler intrinsic line model. However, for the case of an FWHM of 2000 km s^{-1} , it can be seen that the overall line profiles for the HLZ and standard models are barely distinguishable. Since velocity broadening and instrumental broadening have a similar effect on the line profile, one implication of this is that for instruments with a spectral resolution that is worse than 2000 km s^{-1} FWHM at 6.4 keV, X-ray spectral data cannot distinguish between the more

accurate HLZ model of the intrinsic Fe $K\alpha$ and Fe $K\beta$ line profiles and the simpler standard model. Thus, the simpler model is adequate for CCD spectra (FWHM $\sim 7000 \text{ km s}^{-1}$ at 6.4 keV), and may also be adequate for *Chandra* High Energy Transmission Grating spectra (FWHM $\sim 1850 \text{ km s}^{-1}$ at 6.4 keV). The simpler model is not adequate for spectra from X-ray microcalorimeters, which typically have a spectral resolution at 6.4 keV of $\sim 200\text{--}350 \text{ km s}^{-1}$ FWHM. However, the details will depend on the signal-to-noise ratio of the data, and the equivalent widths (EWs) of the Fe $K\alpha$ and Fe $K\beta$ lines. Weaker observed lines will be less sensitive to the accuracy

of the intrinsic line profile model. In order to assess the impact of using the HLZ intrinsic line profiles compared to the standard model, instrumental broadening should be included along with velocity broadening. Some quantitative example are presented in Section 4.

4 EFFECTS OF MICROCALORIMETER INSTRUMENTAL BROADENING

In this section, we illustrate the differences between using the more accurate H97 intrinsic Fe $K\alpha$ and Fe $K\beta$ line profiles, compared to using the simple prescription that is currently used, by spectral-fitting simulated X-ray microcalorimeter spectra with the two models. For the H97 intrinsic profiles, we used the new HLZ MYTORUS line table, and for the simple profiles, we used the standard MYTORUS line table. For the spectral response functions, we used publicly available files that are based on the *Hitomi* soft X-ray spectrometer microcalorimeter (Kilbourne et al. 2018), but were also made available for simulations for the *Resolve* microcalorimeter aboard the X-ray imaging and spectroscopy mission (*XRISM*).³ The line-spread function (LSF) file is `resolve_h5ev_2019a.rmf`, and the effective area file is `resolve_pnt_spec_noGV_20190611.arf`. The LSF has an FWHM of 5 eV, corresponding to 234 km s^{-1} at 6.4 keV, and the effective area at 6.4 keV is 280 cm^2 . The actual FWHM and effective area for *XRISM* data will depend on data extraction details and the final calibration. Clearly, there is also a large variety in the astrophysical source models that will be encountered, as well as in exposure times and source fluxes. The specific model and data for a given analysis scenario should be investigated case by case, with the appropriate calibration. However, the four examples we give will serve as a general guide. For future missions with greater effective area, the corresponding exposure times or source fluxes can be estimated by scaling by the ratio of effective areas at 6.4 keV. For example, for the *Athena* mission, from fig. 4 in Barret et al. (2023), the ratio of the 6.4 keV effective area to that in the simulations is ~ 4.3 . The simulations and spectral fitting described below were performed using XSPEC.

4.1 Case 1

In this example, we use the MYTORUS model in a configuration that generates a ‘pure reflection’ spectrum. The observed spectrum has no direct X-ray continuum (it is blocked), and only the Compton-scattered continuum from a Compton-thick torus observed face-on is observed. The column density is 10^{25} cm^{-2} , and the intrinsic continuum power-law index is 1.9. In this extreme example, the Fe $K\alpha$ line has a prominent Compton shoulder, and the EW is maximal (of the order of $\sim 1 \text{ keV}$), because the line is observed against only the reflected X-ray spectrum. The X-ray spectrum of the Circinus galaxy is an example of a source with this kind of X-ray spectrum (e.g. Kayal et al. 2023, and references therein). The exposure time is 10^5 s , and the normalization of the model is such that the 2–10 keV observed flux is $5 \times 10^{-11} \text{ erg cm}^{-2} \text{ s}^{-1}$ (the latter is typical for an X-ray bright active galaxy). The data are simulated using the new HLZ MYTORUS line table model described in Section 2. We included velocity broadening with an FWHM of 300 km s^{-1} , and set the velocity shift to 0. The model expression in XSPEC is:

$$\text{model} = \text{gsmooth} < 1 > (\text{atable}\{\text{mytorus_scatteredH500_v00.fits}\} < 2 > + \text{atable}\{\text{mytl.V000HLZnEp000_v00.fits}\} < 3 >). \quad (1)$$

The data were then re-fitted in the 6.0–7.5 keV band with the MYTORUS model using the simpler, standard line table. The XSPEC

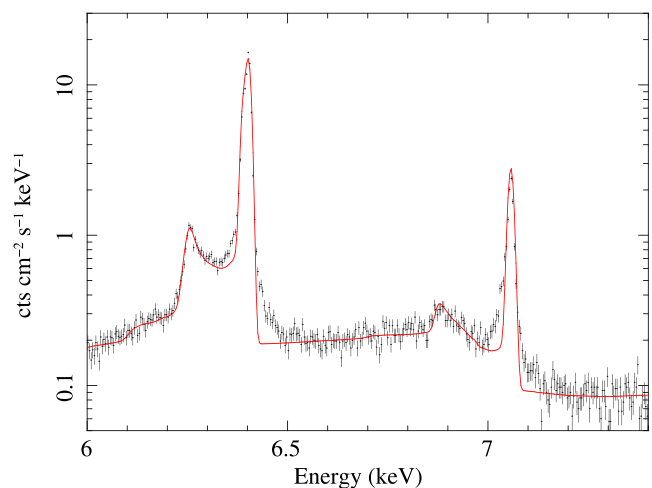


Figure 4. The effects of fitting a pure reflection spectrum simulated with H97 intrinsic Fe $K\alpha$ and Fe $K\beta$ intrinsic line profiles (black) with a model that uses the simpler, standard Gaussian intrinsic line profiles (red). The MYTORUS model is used for both the simulated data and the fitted model, with $N_{\text{H}} = 10^{25} \text{ cm}^{-2}$ and an inclination angle of 0° . The simulated data were made with an LSF that has an FWHM of 5 eV (equivalent to $\sim 234 \text{ km s}^{-1}$ at 6.4 keV), and with velocity broadening that has an FWHM of 300 km s^{-1} . The exposure time was 10^5 s , for an observed 2–10 keV flux of $5 \times 10^{-11} \text{ erg cm}^{-2} \text{ s}^{-1}$, using the spectral response described in the text. The simpler model was fitted with the same LSF, but with the FWHM of the velocity broadening a free parameter. The fitted model also had an additional velocity shift as a free parameter. See text for details, and Fig. 5 for the statistical constraints on the velocity broadening and velocity shift that result from fitting the model with the simpler intrinsic line profiles to the data that were simulated using the more realistic H97 intrinsic line profiles.

model expression is:

$$\text{model} = \text{gsmooth} < 1 > (\text{atable}\{\text{mytorus_scatteredH500_v00.fits}\} < 2 > + \text{atable}\{\text{mytl.V000010nEp000H500_v00.fits}\} < 3 >). \quad (2)$$

The column density and the intrinsic continuum photon index were kept fixed at their input values during the re-fitting process because in the fitted bandpass, the data are not sensitive to these parameters. In a real data analysis workflow, one would fit a more complete model over a wider bandpass. However, the Fe $K\alpha$ and Fe $K\beta$ lines are narrow features, and spectral-fitting over a wider bandpass should not significantly affect constraints on their widths. Thus, there were three free parameters in the fit: the overall normalization, the velocity broadening FWHM, and the velocity shift.

The simulated data overlaid with the re-fitted simpler model are shown in Fig. 4. It can be seen that the fit fails to capture the correct shapes of the ‘wings’ of both the Fe $K\alpha$ line, and the Fe $K\beta$ line. The line cores and the Compton shoulders of both lines are fitted adequately, but at a cost: the required velocity broadening is much larger than that which was input into the simulated data. This is illustrated in Fig. 5, which shows the 68 per cent, 90 per cent, and 99 per cent confidence contours for the velocity broadening FWHM versus the velocity shift of the line spectrum. Although it is invalid to construct confidence contours for a poor fit, they nevertheless serve as a guide. It can be seen that the FWHM is overestimated by a factor of more than 2, and the smallest value of the 99 per cent confidence contour is $\sim 670 \text{ km s}^{-1}$. There is also a systematic velocity redshift that is clearly an artefact of using the simpler model of the line profiles, since the velocity shift in the simulated data is 0. The 99 per cent confidence contour from the data re-fitted with the simpler model shows a very narrow range of the velocity redshift,

³<https://heasarc.gsfc.nasa.gov/docs/xrism/proposals/>

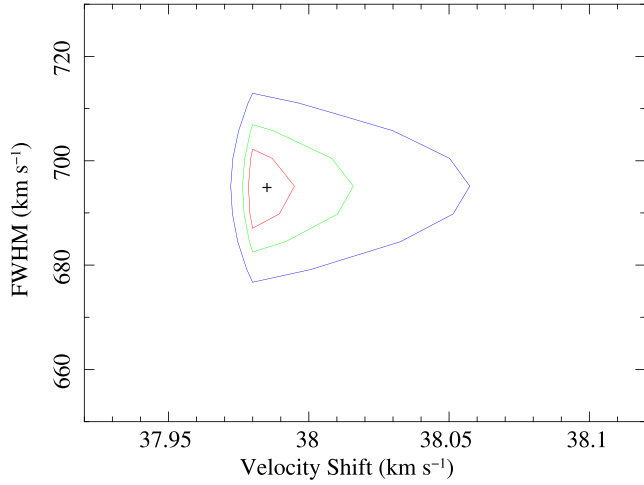


Figure 5. The 68 per cent, 90 per cent, and 99 per cent confidence contours of Fe K α and Fe K β line velocity broadening FWHM versus velocity shift, corresponding to the spectral fit in Fig. 4. Positive velocity shifts correspond to redshifted energies. The confidence contours show that fitting data that were simulated using H97 intrinsic line profiles, with the oversimplified Gaussian intrinsic line profiles, significantly overestimates the velocity broadening (by more than a factor of 2 in this case). The velocity broadening FWHM of the simulated data was 300 km s⁻¹, but it can be seen that even the 99 per cent contour excludes this value. There is also an apparent non-zero velocity shift that is an artefact of fitting the simpler line profile model.

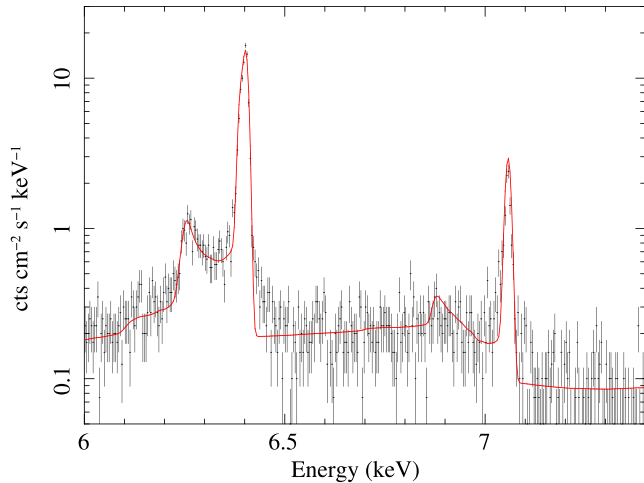


Figure 6. As Fig. 4, except that the exposure time is reduced by a factor of 10 (or equivalently, the 2–10 keV flux is reduced by a factor of 10).

with minimum and maximum values of 37.97 and 38.06 km s⁻¹, respectively.

4.2 Case 2

For this case, the procedures and models are identical to those for case 1. The difference is that the exposure time was reduced by an order of magnitude, to 10⁴ s. This is also equivalent to keeping the exposure time at 10⁵ s, but reducing the observed flux by an order of magnitude. The simulated data overlaid with the re-fitted simpler model are shown in Fig. 6. It can be seen that although the statistical quality of the data is poorer, an excess on the blue wing of the Fe K α line is still apparent, but the excess on the blue wing of the Fe K β line is not so prominent. Both lines still also show signs of a weak

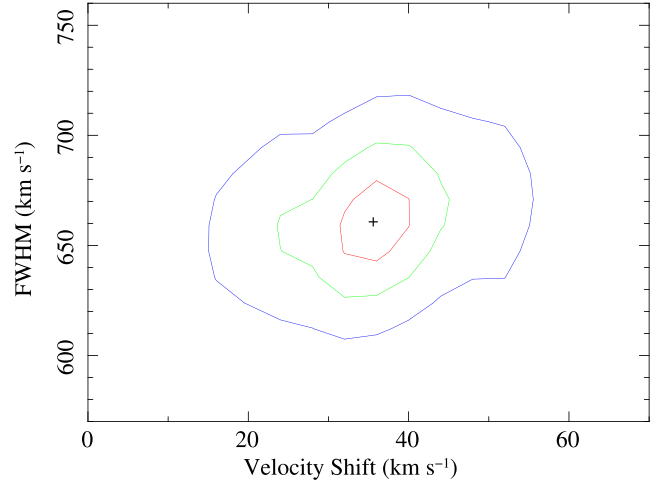


Figure 7. The 68 per cent, 90 per cent, and 99 per cent confidence contours of Fe K α and Fe K β line velocity broadening FWHM versus velocity shift, corresponding to the spectral fit in Fig. 6. Positive velocity shifts correspond to redshifted energies. Even though the simulated data have much larger statistical errors than the spectrum in Fig. 4 (simulated with the same model) due to an order of magnitude decrease in the exposure time, the 99 per cent confidence contours still overestimate the FWHM by a factor ~ 2 , excluding the value of 300 km s⁻¹ that was used for the simulated data. There is still an apparent velocity shift (corresponding to redshifted line energies), of ~ 38 km s⁻¹, but the constraints are much looser than they are for case 1.

excess on the red wings. Fig. 7 shows the 68 per cent, 90 per cent, and 99 per cent confidence contours for the velocity broadening FWHM versus the velocity shift of the line spectrum. It can be seen that even with poorer quality data, the FWHM of Fe K α and Fe K β emission lines is still overestimated by more than a factor of 2. The lowest value of the 99 per cent lower limit on the FWHM is more than ~ 600 km s⁻¹. The apparent velocity redshift of ~ 36 km s⁻¹ is also similar to that obtained for case 1, except that the constraints are much looser. The 99 per cent confidence range in the velocity shift is ~ 15 – 55 km s⁻¹.

4.3 Case 3

For this case, the model is a Compton-thin torus observed face-on, with the direct, intrinsic power-law continuum unblocked. The XSPEC model expression for the simulation model with the HLZ line profiles is:

$$\begin{aligned} \text{model} = & \text{gsmooth} < 1 > (\\ & \text{zpowerlw} < 2 > * \text{etable}\{\text{mytorus_Ezero_v00.fits}\} < 3 > + \\ & \text{atable}\{\text{mytorus_scatteredH500_v00.fits}\} < 4 > + \\ & \text{atable}\{\text{mytl_V000HLZnEp000_v00.fits}\} < 5 >). \end{aligned} \quad (3)$$

The column density is 10²³ cm⁻², and all other parameters and procedures are the same as for case 1. However, the Fe K α and Fe K β lines are now weak against the net continuum, and there is essentially no Compton shoulder. The EW of the Fe K α line is only 25 eV. The XSPEC expression for the simpler model with the standard line profiles is:

$$\begin{aligned} \text{model} = & \text{gsmooth} < 1 > (\\ & \text{zpowerlw} < 2 > * \text{etable}\{\text{mytorus_Ezero_v00.fits}\} < 3 > + \\ & \text{atable}\{\text{mytorus_scatteredH500_v00.fits}\} < 4 > + \\ & \text{atable}\{\text{mytl_V000010nEp000H500_v00.fits}\} < 5 >). \end{aligned} \quad (4)$$

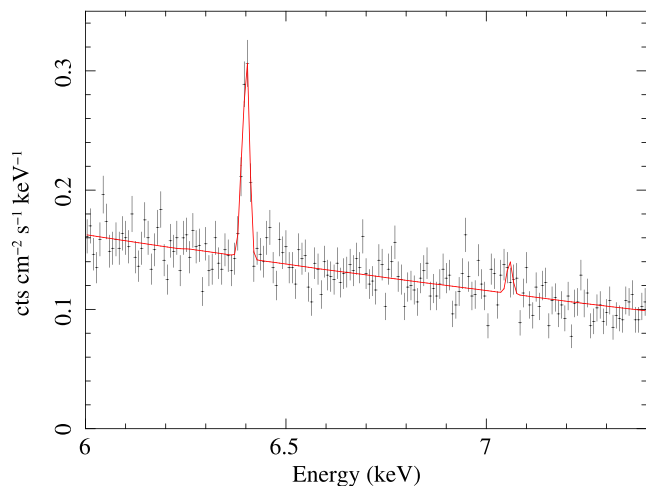


Figure 8. The effects of fitting a typical Compton-thin spectrum, that was simulated with H97 intrinsic Fe $K\alpha$ and Fe $K\beta$ intrinsic line profiles (black), with a model that uses the simpler, standard Gaussian intrinsic line profiles (red). The MYTORUS model is used for both the simulated data and the fitted model, with $N_H = 10^{23} \text{ cm}^{-2}$ and an inclination angle of 0° . The simulated data were made with an LSF that has an FWHM of 5 eV (equivalent to $\sim 234 \text{ km s}^{-1}$ at 6.4 keV), and velocity broadening that has an FWHM of 300 km s^{-1} . The exposure time was 10^5 s , for an observed 2–10 keV flux of $5 \times 10^{-11} \text{ erg cm}^{-2} \text{ s}^{-1}$, using the spectral response described in the text. The model was fitted with the same LSF, but with the FWHM of the velocity broadening a free parameter. The fitted model also had an additional velocity shift as a free parameter. See text for details, and Fig. 9 for the statistical constraints on the velocity broadening and velocity shift that result from fitting the model with the simpler intrinsic line profiles to the data that were simulated using the more realistic H97 intrinsic line profiles.

The simulated data overlaid with the re-fitted simpler model are shown in Fig. 8. It can be seen that the data are fitted well. However, as for cases 1 and 2, there is a cost: the required velocity broadening is much larger than that which was input into the simulated data. This is illustrated in Fig. 9, which shows the 68 per cent, 90 per cent, and 99 per cent confidence contours for the velocity broadening FWHM versus the velocity shift of the line spectrum. It can be seen that the FWHM is still overestimated by a factor ~ 2 , but the smallest value of the 99 per cent confidence contour is $\sim 380 \text{ km s}^{-1}$. The velocity shift is consistent with 0.

4.4 Case 4

For this case, the procedures and models are identical to those for case 3. The difference is that the exposure time was reduced by an order of magnitude, to 10^4 s . This is also equivalent to keeping the exposure time at 10^5 s , but reducing the observed flux by an order of magnitude. The simulated data overlaid with the re-fitted simpler model are shown in Fig. 10. It can be seen that the statistical quality of the data is so poor that the Fe $K\alpha$ line is barely detectable, and the Fe $K\beta$ line is not detected. Fig. 11 shows the 68 per cent, 90 per cent, and 99 per cent confidence contours for the velocity broadening FWHM versus the velocity shift of the line spectrum. It can be seen that now the input FWHM of $\sim 300 \text{ km s}^{-1}$ is not ruled out by the 99 per cent confidence contour, and that the velocity shift is still consistent with 0. However, the 99 per cent confidence contour is very large, extending up to an FWHM of $\sim 3000 \text{ km s}^{-1}$.

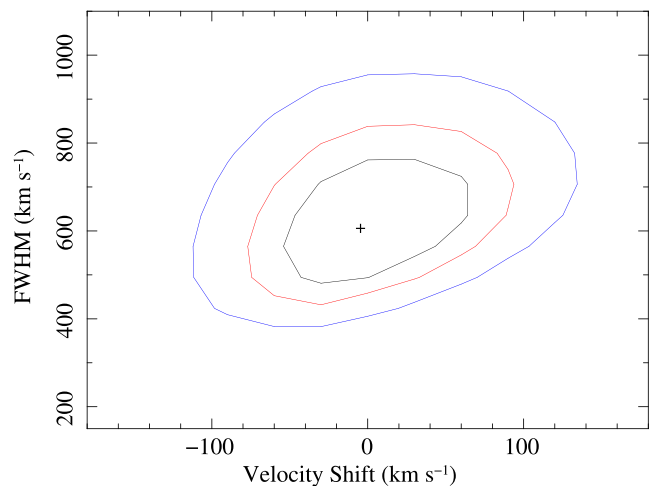


Figure 9. The 68 per cent, 90 per cent, and 99 per cent confidence contours of Fe $K\alpha$ and Fe $K\beta$ line velocity broadening FWHM versus velocity shift, corresponding to the spectral fit in Fig. 8. Positive velocity shifts correspond to redshifted energies. The confidence contours show that fitting data that were simulated using H97 intrinsic line profiles with the oversimplified Gaussian intrinsic line profiles overestimate the velocity broadening, even when the Fe $K\alpha$ line is weak (in this case the EW of that line is $\sim 25 \text{ eV}$). The velocity broadening FWHM of the simulated data was 300 km s^{-1} , but it can be seen that even the 99 per cent contour excludes this value. However, the velocity shift is consistent with 0.

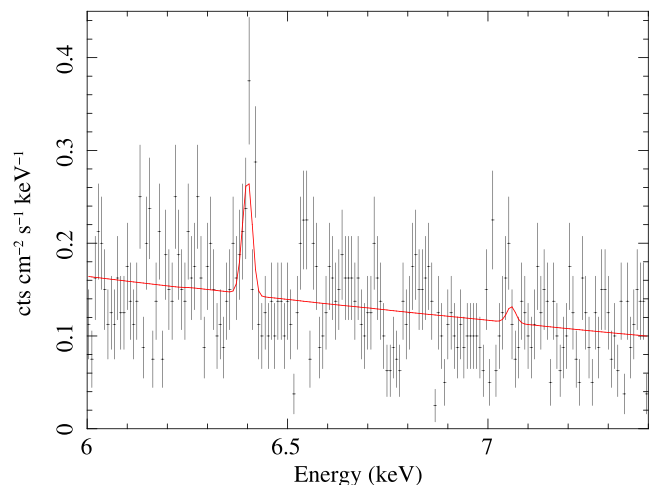


Figure 10. As Fig. 8, except that the exposure time is reduced by a factor of 10 (or equivalently, the 2–10 keV flux is reduced by a factor of 10).

5 SUMMARY

We have calculated a new Fe $K\alpha$ and Fe $K\beta$ emission-line table for the MYTORUS X-ray reprocessor spectral-fitting model. The MYTORUS model is based on Monte Carlo simulations, and the new line spectrum utilizes the high-precision intrinsic line profile measurements reported by Hölzer et al. (1997). The new line table can be used seamlessly for spectral-fitting X-ray spectra with the MYTORUS model by replacing the existing line table with it. In addition, the new model can also be used in a standalone mode, without an associated physical model. This is useful for initially diagnosing an X-ray spectrum with empirical fits, in order to estimate line widths that are corrected for instrumental broadening.

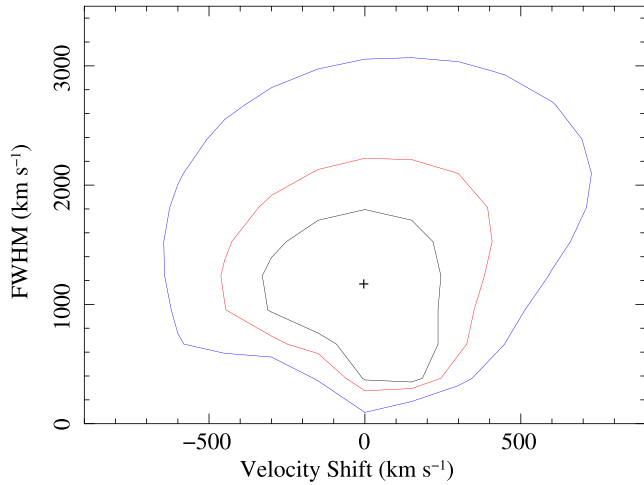


Figure 11. The 68 per cent, 90 per cent, and 99 per cent confidence contours of Fe K α and Fe K β line velocity broadening FWHM versus velocity shift, corresponding to the spectral fit in Fig. 10. Positive velocity shifts correspond to redshifted energies. Since the simulated data have much larger statistical errors than the spectrum in Fig. 8 (simulated with the same model) due to an order of magnitude decrease in the exposure time, the 99 per cent confidence contours now include the FWHM of 300 km s $^{-1}$ that was used for the simulated data. However, the 99 per cent confidence upper contour does not rule out an FWHM as large as 3000 km s $^{-1}$. The velocity shift is consistent with 0, but the constraints on it are also loose, with the 99 per cent confidence contour extending to $\sim \pm 650$ km s $^{-1}$.

We illustrated the effects of velocity broadening on the newly implemented intrinsic line spectrum, with and without instrumental broadening (the latter was based on an X-ray microcalorimeter detector, similar to that onboard *XRISM*). Since the laboratory-based line profiles are broader than the simplistic Gaussian line profiles that are currently used, the new table will yield smaller astrophysical line widths than the standard, simplistic approach does, if the ‘true’ FWHM of the Fe K α line, due to non-intrinsic broadening in the source, is less than ~ 2000 km s $^{-1}$. However, the ability of the data to distinguish between the simple and complex intrinsic line profile models depends on the signal-to-noise ratio of the spectral data, and the EWs of the Fe K α and Fe K β emission lines. Individual scenarios should be investigated case by case. Some potential consequences of using the oversimplified approach to represent intrinsic line widths are the appearance of residual red and blue wings on the Fe K α and Fe K β emission lines, and an overestimate of the velocity broadening FWHM by as much as a factor of ~ 2 . We found that the Compton shoulders of the Fe K α and Fe K β lines, when present, are less sensitive than the line cores to the intrinsic line profile shapes, even for the extremal case of a Compton-thick, ‘pure’ X-ray reflection spectrum.

ACKNOWLEDGEMENTS

This work was supported by National Aeronautics and Space Administration (NASA) grants NNX10AE83G and 80GSFC21M0002. This research has made use of data and software provided by the High Energy Astrophysics Science Archive Research Center (HEASARC), which is a service of the Astrophysics Science Division at NASA/Goddard Space Flight Center and the High Energy Astrophysics Division of the Smithsonian Astrophysical Observatory.

DATA AVAILABILITY

The data underlying this article will be shared on reasonable request to the corresponding author.

REFERENCES

- Andonie C. et al., 2022, *A&A*, 664, A46
 Arnaud K. A., 1996, in Jacoby G., Barnes J., eds, *ASP Conf. Ser. Vol. 101*, *Astronomical Data Analysis Software and Systems V*. Astron. Soc. Pac., San Francisco, p. 17
 Baloković M. et al., 2018, *ApJ*, 854, 42
 Barret D. et al., 2023, *Exp. Astron.*, 55, 373
 Brightman M., Nandra K., 2011, *MNRAS*, 413, 1206
 Buchner J., Brightman M., Nandra K., Nikutta R., Bauer F. E., 2019, *A&A*, 629, A16
 Furui S., Fukazawa Y., Odaka H., Kawaguchi T., Ohno M., Hayashi K., 2016, *ApJ*, 818, 164
 Harrison F. A. et al., 2013, *ApJ*, 770, 103
 Hikitani M., Ohno M., Fukazawa Y., Kawaguchi T., Odaka H., 2018, *ApJ*, 867, 80
 Hölzer G., Fritsch M., Deutsch M., Härtwig J., Förster E., 1997, *Phys. Rev. A*, 56, 4554
 Ikeda S., Awaki H., Terashima Y., 2009, *ApJ*, 692, 608
 Kayal A., Singh V., Ricci C., Mithun N. P. S., Vadawale S., Dewangan G., Gandhi P., 2023, *MNRAS*, 522, 4098
 Kilbourne C., et al., 2018, *J. Astron. Telesc. Instrum. Syst.*, 4, 011214
 Koyama K. et al., 2007, *PASJ*, 59, 23
 LaMassa S. M., Yaqoob T., Ptak A. F., Juanjun J., Heckman T. M., Ghandi P., Urry C. M., 2014, *ApJ*, 787, 61
 Liu Y., Li X., 2014, *ApJ*, 787, 52
 Lubiński P., Zdziarski A. A., 2001, *MNRAS*, 323, L37
 Markert T. H., Canizares C. R., Dewey D., McGuirk M., Pak C. S., Shattenburg M. L., 1994, in Siegmund O. H. W., Vallerga J. V., eds, *Proc. SPIE Conf. Ser. Vol. 2280*, *EUV, X-Ray, and Gamma-Ray Instrumentation for Astronomy V*. SPIE, Bellingham, p. 168
 Matt G., Bianchi S., Guainazzi M., Molendi S., 2004, *A&A*, 414, 155
 Miller J. M., Kammoun E., Ludlam R. M., Gendreau K., Arzoumanian Z., Cackett E., Tombesi F., 2019, *ApJ*, 884, 106
 Murphy K. D., Yaqoob T., 2009, *MNRAS*, 397, 1549
 Nobukawa M., Uchiyama H., Nobukawa K. K., Yamauchi S., Koyama K., 2016, *ApJ*, 833, 268
 Odaka H., Yoneda H., Takahashi T., Fabian A., 2016, *MNRAS*, 462, 2366
 Pradhan P., Raman G., Paul B., 2019, *MNRAS*, 483, 5687
 Saha T., Markowitz A. G., Buchner J., 2022, *MNRAS*, 509, 5485
 Shu X. W., Yaqoob T., Wang J. X., 2010, *ApJ*, 718, 581
 Shu X. W., Yaqoob T., Wang J. X., 2011, *ApJ*, 738, 147
 Sulentic J. W., Marziani P., Zwitter T., Calvani M., Dultzin-Hacyan D., 1998, *ApJ*, 501, 54
 Tanimoto A., Ueda Y., Odaka H., Kawaguchi T., Fukazawa Y., Kawamuro T., 2019, *ApJ*, 877, 95
 Torrejón J. M., Schulz N. S., Nowak M. A., Kallman T. R., 2010, *ApJ*, 715, 947
 Tzanavaris P., Yaqoob T., 2018, *ApJ*, 855, 25
 Yaqoob T. et al., 2007, *PASJ*, 59, 283
 Yaqoob T., 2012, *MNRAS*, 423, 3360
 Yaqoob T., Murphy K. D., 2011, *MNRAS*, 412, 277
 Yaqoob T., Padmanabhan U., 2004, *ApJ*, 604, 73
 Yaqoob T., Tatum M. M., Scholtes A., Gottlieb A., Turner T. J., 2015, *MNRAS*, 454, 973
 Yaqoob T., Turner T. J., Tatum M. M., Trevor M., Scholtes A., 2016, *MNRAS*, 462, 4038
 Yaqoob T., Tzanavaris P., LaMassa S., 2023, *MNRAS*, 522, 394

This paper has been typeset from a \LaTeX file prepared by the author.